

# Functional Carbon Interlayer with Indium Oxide-Rich Nanoparticles for High-Performance Lithium–Sulfur Batteries

Ting Ma<sup>+</sup><sup>[a]</sup> Yibo Xiao<sup>+</sup><sup>[a]</sup> Xiaoxia Lv,<sup>[a]</sup> Haixia Yue,<sup>[a]</sup> Yixin Huang,<sup>[a]</sup> Xin Li,<sup>[a]</sup> Na He,<sup>[b]</sup> Changzhen Zhan,<sup>[c]</sup> Yu Bai,<sup>\*[d]</sup> and Ding Nan<sup>\*[a]</sup>

Lithium–sulfur batteries are gaining a lot of attention from researchers due to their high energy density, high theoretical specific capacity, and low raw material prices. Nevertheless, the dissolution and diffusion of certain polysulfides during charge and discharge cycles result in a shuttle effect, while reduced sulfur utilization remains a barrier to their commercial viability. In this study, we propose the use of carbon nanofibers enriched with indium oxide nanoparticles (be called  $\text{In}_2\text{O}_3@\text{CNF}$ ) as a functional interlayer for lithium–sulfur batteries. The interlayer of this innovation serves a dual purpose. Indium oxide nanoparticles can adsorb polysulfide to inhibit the shuttle effect, and

accelerate the catalytic transformation of polysulfide to enhance the reaction kinetics. As a result, the electrochemical performance of the battery with the  $\text{In}_2\text{O}_3@\text{CNF}$  interlayer exhibited remarkable improvements. The initial discharge capacity was  $1187 \text{ mAh g}^{-1}$  at  $0.2 \text{ C}$  and the capacity retention was 77.5% after 100 cycles. Furthermore, even at a higher current density of  $1 \text{ C}$ , the battery demonstrated a substantial initial capacity of  $997 \text{ mAh g}^{-1}$ , maintaining a capacity retention of  $589 \text{ mAh g}^{-1}$  after 400 cycles. Notably, the battery exhibited stable Coulombic efficiency (CE) and minimal single-cycle capacity decay (0.1%).

## 1. Introduction

With the advancement of modern science and technology, electronic devices are continuously evolving towards lightweight, portable, and miniaturized forms. Consequently, there is a growing demand for lightweight and high-energy-density batteries.<sup>[1–4]</sup> Traditional lithium-ion batteries, due to their intrinsic limitations, struggle to meet these demands. Lithium–sulfur batteries (Li–S batteries), on the other hand, are considered an ideal candidate for the next-generation energy storage systems because of their exceptionally high theoretical energy density ( $1675 \text{ mAh g}^{-1}$ ) enabled by the multi-electron reaction ( $\text{S}_8 + 16 \text{ Li}^+ + 16 \text{ e}^- = 8 \text{ Li}_2\text{S}$ ).<sup>[5–8]</sup> However, Li–S batteries face several major challenges that hinder their commercialization. These challenges include: 1) Sulfur and discharge product  $\text{Li}_2\text{S}$  are electrically insulating, resulting in low utilization of

active materials.<sup>[9,10]</sup> 2) During the electrochemical reaction process, Li–S batteries produce intermediate products, polysulfides, which dissolve and shuttle to the anode, causing parasitic reactions with lithium metal.<sup>[11]</sup> 3) The expansion of electrode volume during charge and discharge processes makes the electrodes prone to cracking. 4) The lithium metal anode interface is unstable, leading to dendrite formation and safety concerns.<sup>[12–15]</sup>

To address the challenges associated with sulfur cathodes, researchers have developed various strategies, including, constructing carbon-based<sup>[16,17]</sup> and non-carbon-based<sup>[18,19]</sup> hosts to enhance sulfur conductivity, and creating functional interlayers and separators to inhibit polysulfide dissolution.<sup>[20]</sup> These components play a crucial role in mitigating the diffusion of polysulfides between the cathode and anode. Functional interlayers and separators are designed to suppress the shuttling of lithium polysulfides, which helps maintain the integrity of the battery. Another strategy involves developing functional electrolytes.<sup>[21,22]</sup> Functional electrolytes can modulate the composition of SEI and inhibit dendrite growth. In addition, nanoscale electrode materials with extremely high specific surface area and controllable pore structure can be obtained through electrostatic spinning technology, which can provide more active surfaces and better ion transport paths, which make them widely applicable in batteries.<sup>[23–28]</sup> For example, Wu et al.<sup>[29]</sup> utilized electrostatically spun carbide nanofiber films as an interlayer for Li–S batteries. The mesh-like and microporous structure of this interlayer not only enhanced the conductivity of the sulfur cathode but also effectively mitigated the shuttle effect. Similarly, Liang et al.<sup>[30]</sup> employed the electrospinning method to decorate ultrafine  $\text{TiO}_2$  nanoparticles onto carbon nanofibers (CNFs), creating a functional CNF-T interlayer that

[a] T. Ma,<sup>+</sup> Y. Xiao,<sup>+</sup> X. Lv, H. Yue, Y. Huang, X. Li, D. Nan  
School of Chemistry and Chemical Engineering, Inner Mongolia University, Hohhot, 010021, China  
E-mail: nan1980732@163.com

[b] N. He  
Inner Mongolia Institute of Metrology and Testing, Hohhot, 010050, China

[c] C. Zhan  
State Key Laboratory of New Ceramics and Fine Processing, School of Materials Science and Engineering, Tsinghua University, Beijing 100084, China

[d] Y. Bai  
Shanghai XFH Technology Co. Ltd., Building A7, No. 11, Lane 635, Xiaoyun Road, Baoshan District, Shanghai 200949, China  
E-mail: yubaicn@163.com

[+] These authors contributed equally to this work.

Supporting information for this article is available on the WWW under <https://doi.org/10.1002/batt.202400726>

mitigated volume expansion and shuttle effect in Li-S batteries. The ultrafine TiO<sub>2</sub> nanoparticles on CNFs serve as anchors, capturing polysulfides through strong interactions, thereby bestowing the battery with significantly improved electrochemical stability. Similarly, Cho et al.<sup>[31]</sup> prepared nitrogen-doped carbon nanofibers (P–N–C NFs) with hierarchical pore structure, incorporating VN nanodots as chemisorption sites for effective anchoring of lithium polysulfides. Overall, the interlayer significantly improves the comprehensive performance of Li-S batteries due to its unique structure and functionalization.

The electrons located near the oxygen defects in metal oxides are highly reactive, allowing them to readily chemisorb with polysulfide molecules and form robust covalent bonds, effectively restraining the shuttle effect caused by polysulfide dissolution.<sup>[32–34]</sup> Indium oxide (In<sub>2</sub>O<sub>3</sub>) is a widely used material with applications in various fields, including batteries, touchscreens, and gas sensors.<sup>[35]</sup> Compared to other oxides, indium oxide has excellent electrical conductivity and electrocatalytic properties as well as strong polysulfide adsorption capability.<sup>[36]</sup> Ho et al.<sup>[37]</sup> obtained In<sub>2</sub>O<sub>3</sub> films through electrochemical deposition and employed them as the anode material for lithium-ion batteries. In 2020, Han et al.<sup>[38]</sup> utilized an indium-based metal-organic framework (MOF) called CPM-5 as a precursor, followed by carbonization at 600 °C to produce a composite cathode for Li-S batteries. The In<sub>2</sub>O<sub>3</sub> particles formed during carbonization combined with CPM-5 to create a core-shell structure. The assembled battery exhibited exceptional rate performance. Wang et al.<sup>[39]</sup> presents a novel In<sub>2</sub>O<sub>3</sub>@C modified separator material designed to enhance the performance of Li-S batteries, particularly by suppressing the shuttle effect of lithium polysulfides and accelerating their redox kinetics. This results in excellent stability and reversibility of the battery under high current and low-temperature conditions.

In this study, we opted for In<sub>2</sub>O<sub>3</sub> and chose polyacrylonitrile (PAN) as the carbon framework. Utilizing the electrospinning technique, we embedded In<sub>2</sub>O<sub>3</sub> nanoparticles into carbon fibers, resulting in the fabrication of an In<sub>2</sub>O<sub>3</sub>@CNF composite interlayer material. Carbon nanofibers have excellent electrical conductivity, which will improve the conductivity of the host. In<sub>2</sub>O<sub>3</sub> nanoparticles will disperse across the carbon fibers, providing an abundance of active sites that can anchor polysulfides and alleviate the shuttle effect. The Li-S battery with the In<sub>2</sub>O<sub>3</sub>@CNF interlayer delivered an outstanding initial discharge capacity of 1187.4 mAh g<sup>-1</sup> at a current density of 0.2 C. After 100 cycles, it retained a discharge capacity of 920.5 mAh g<sup>-1</sup>. Even at a higher discharge rate of 1 C, it exhibited not only an impressive initial discharge capacity of 997 mAh g<sup>-1</sup> but also exceptional cycling stability with a coulombic efficiency close to 100% after 400 cycles.

## Experimental Section

### Preparation of C/S Electrode

The multi-walled carbon nanotubes and S powder were purchased from Sigma Aldrich. The multi-walled carbon nanotubes and S

powder were mixed and ground at a mass ratio of 1:4 for 30 min. The C/S powder was poured into the reaction kettle, and the temperature was increased to 155 °C at 2 °C·min<sup>-1</sup>, and the C/S composite was obtained after 12 h of heat preservation. The S mass share of the C/S composite is 77%. (Figure S1) To make a low mass loading C/S composite electrode, C/S composite, Super-P, and polyvinylidene fluoride (PVDF) were mixed with a mass ratio of 8:1:1 in N-methyl pyrrolidone (NMP), and then the slurry was cast on the Al foil and dried at 60 °C under vacuum for 12 h. The areal loading of active materials (S) is about 2 mg cm<sup>-2</sup>. The high loading capacity of the electrode areal loading is about 6 mg cm<sup>-2</sup>.

### Preparation of In<sub>2</sub>O<sub>3</sub>@CNF Films

Polyacrylonitrile (PAN) was purchased from Sigma Aldrich, M.w. ~150,000.) (1 g) was dissolved in 9 mL of N,N-dimethylformamide (DMF) and stirred at 60 °C for 5 hours to obtain a transparent PAN solution. Then, 1 g of indium nitrate (In(NO<sub>3</sub>)<sub>3</sub> purchased from Alfa Aesar) was added and continuously stirred at 60 °C until fully dissolved. The mixed solution was poured into a 20 mL syringe with the plunger speed set to 0.6 mL/h. The distance between the spraying nozzle and the rotary collector was 15 cm, and the voltage was set to 22 kV. Electrospinning was carried out for 5 hours to obtain carbon fibers. After that, the carbon fibers were peeled off from the collector and dried overnight at 60 °C in a drying oven. The carbon fibers were then placed in a blast drying oven for low-temperature pre-oxidation treatment. Under air atmosphere, the temperature was raised from 25 °C to 200 °C at a heating rate of 2 °C/min and held for 1 hour. After pre-oxidation was completed, the carbon fibers were taken out of the blast drying oven and placed in a tube furnace, where high-temperature carbonization was carried out under Ar atmosphere. The temperature was raised from 25 °C to 650 °C at 5 °C/min and held for 3 hours to complete carbonization, thus obtaining In<sub>2</sub>O<sub>3</sub>@CNF films.

### Characterizations

The XRD patterns were collected using a Rigaku SmartLab diffractometer with Cu K $\alpha$  radiation ( $\lambda = 1.5405 \text{ \AA}$ ) in a scan range (2 $\theta$ ) of 5–90°. SEM images and EDS of In<sub>2</sub>O<sub>3</sub>@CNF films were obtained by HITACHI-SU8220 type field emission scanning electron microscope. The TEM used is Tecnai G2 F30 model from FEI Company in USA. XPS was applied to analyze the surface chemical bonding states of In<sub>2</sub>O<sub>3</sub>@CNF films. The BET tests were conducted using a BEL sorp-minill physisorption analyzer manufactured by BEL Japan. The specific surface area and pore structure characteristics of the materials were obtained by N<sub>2</sub> adsorption-desorption analysis.

### Electrochemical Measurements

The 2032-type coin cell was used for C/S || Li cells. The electrolyte was made using 1 M Lithium bis(trifluoromethanesulphonyl)imide (LiTFSI) + 2% LiNO<sub>3</sub> dissolved in 1,3-Dioxolane (DOL) and 1,2-Dimethoxyethane (DME) (1:1 volume ratio). The amount of electrolyte is 40  $\mu\text{L}$ . The interlayer is always placed between the cathode and the separator. The mass of the interlayer is about 0.2 mg cm<sup>-2</sup>. Galvanostatic charge-discharge tests were conducted within a voltage window of 1.7–2.8 V using battery testers (Wuhan Land CT2001A, China) at 25 °C. The Princeton PMC1000 A electrochemical workstation was used for the EIS test. The test frequency was in the range of 1 mHz–100 kHz, and the amplitude was 5 mV. Galvanostatic intermittent titration technique (GITT) was conducted using a pulse current of 0.1 C for 30 min followed by a relaxation of 30 min.

### Preparation of $\text{Li}_2\text{S}_6$ Solution and Symmetric Cells Tests

Sublimed sulfur and  $\text{Li}_2\text{S}$  powder (with molar ratio of 5:1) were added into a mixture of DOL/DME (1:1, v/v) and stirred at 60°C for 12 h in glovebox to obtain 0.2M  $\text{Li}_2\text{S}_6$  solution. Then the brown solution was diluted to 2 mM with DOL/DME for the polysulfide adsorption test. CV was measured within a voltage range from -0.8 to 0.8V at scan rate of 10 mV s<sup>-1</sup>.

## 2. Results and Discussion

Indium nitrate and polyacrylonitrile were spun into fibers by using electrostatic spinning. After high temperature treatment, uniform indium oxide nanoparticles were formed on the carbon nanofibers. The preparation process and principle of  $\text{In}_2\text{O}_3@\text{CNF}$  is shown in Figure 1. Figure 2(a) and (d) show the SEM images of the original CNF film, the fiber surface is smooth with diameter around 200 nm. The mesh structure of carbon fibers provides a good electronically conductive framework to increase electrical conductivity as well as mitigate the volume change of sulfur during charge-discharge cycles. Figure 2(b) and (e) are SEM images of  $\text{In}_2\text{O}_3@\text{CNF}$  film. Compared with CNF, the fiber surface of  $\text{In}_2\text{O}_3@\text{CNF}$  is rough with diameter around 300 nm. As shown in Figure 2(c), further TEM observations reveal that many nanoparticles grew on the carbon fiber surface. Figure 2(g-j) are EDS elemental mapping images of  $\text{In}_2\text{O}_3@\text{CNF}$ , where the mapping of C, In and O elements also confirms the structure of  $\text{In}_2\text{O}_3$  and its uniform dispersion. We attribute this distribution of  $\text{In}_2\text{O}_3$  nanoparticles to the nitrate pyrolysis process. During annealing,  $\text{In}(\text{NO}_3)_3$  decomposed into  $\text{In}_2\text{O}_3$ ,  $\text{O}_2$  and  $\text{NO}_2$ . As the gases escaped,  $\text{In}_2\text{O}_3$  nucleus and undecomposed  $\text{In}(\text{NO}_3)_3$  moved to the fiber surface, eventually

forming  $\text{In}_2\text{O}_3$  nanoparticles. The lattice fringes of the nanoparticles are clearly shown in Figure 2(f), with interplanar spacings of 0.292 nm and 0.297 nm, consistent with the (222) and (311) planes of  $\text{In}_2\text{O}_3$  crystal lattice. The above results indicate that the small particles grown on the carbon surface are  $\text{In}_2\text{O}_3$ . This unique nanostructure is beneficial for contact with electrolyte and electron transfer, facilitating fast charge-discharge cycles.<sup>[40]</sup>

To investigate the phase compositions of CNF and  $\text{In}_2\text{O}_3@\text{CNF}$ , X-ray diffraction (XRD) spectra were obtained. Figure 3(a) shows the XRD patterns of CNF and  $\text{In}_2\text{O}_3@\text{CNF}$ , where characteristic peaks of amorphous carbon structure appear around 25° for both samples.  $\text{In}_2\text{O}_3@\text{CNF}$  shows a diffraction peak at 30.58°, corresponding to the (222) crystal plane of  $\text{In}_2\text{O}_3$  in the standard PDF card, confirming that the particles on the carbon fibers are  $\text{In}_2\text{O}_3$ , consistent with the EDS analysis. Raman spectra of CNF and  $\text{In}_2\text{O}_3@\text{CNF}$  are shown in Figure 3(b). Both samples exhibit two characteristic peaks of carbon materials, which are the D peak ( $1346 \text{ cm}^{-1}$ ) and G peak ( $1597 \text{ cm}^{-1}$ ). For the  $\text{In}_2\text{O}_3@\text{CNF}$  film, in addition to the two carbon peaks, there are also peaks at 104.6, 126.52 and  $149.4 \text{ cm}^{-1}$ , corresponding to the characteristic peaks of  $\text{In}_2\text{O}_3$  phase. Furthermore, the  $I_{\text{D}}/I_{\text{G}}$  ratio (the ratio of D peak to G peak intensities) is 1.12 for CNF, while it is 1.01 for  $\text{In}_2\text{O}_3@\text{CNF}$ , which is lower than that of CNF. This result indicates that the oxygen defect structure of  $\text{In}_2\text{O}_3$  is introduced into the carbon fibers.<sup>[41]</sup>

X-ray photoelectron spectroscopy (XPS) analysis was performed to further investigate the chemical states and composition of  $\text{In}_2\text{O}_3@\text{CNF}$ . As shown in the full XPS spectrum in Figure S2,  $\text{In}_2\text{O}_3@\text{CNF}$  exhibits characteristic peaks at 284.8 eV, 445.0 eV, 531.5 eV, 666.1 eV and 704.6 eV, corresponding to C1s, In 3d, O 1s, In 3p3 and In 3p1, respectively, verifying the

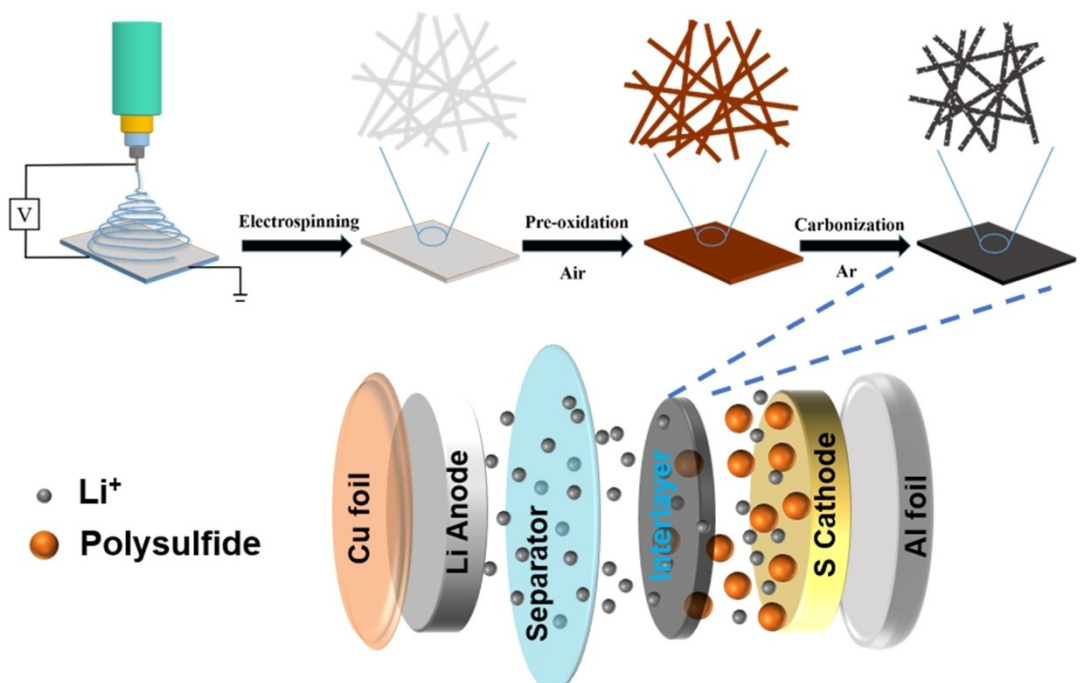
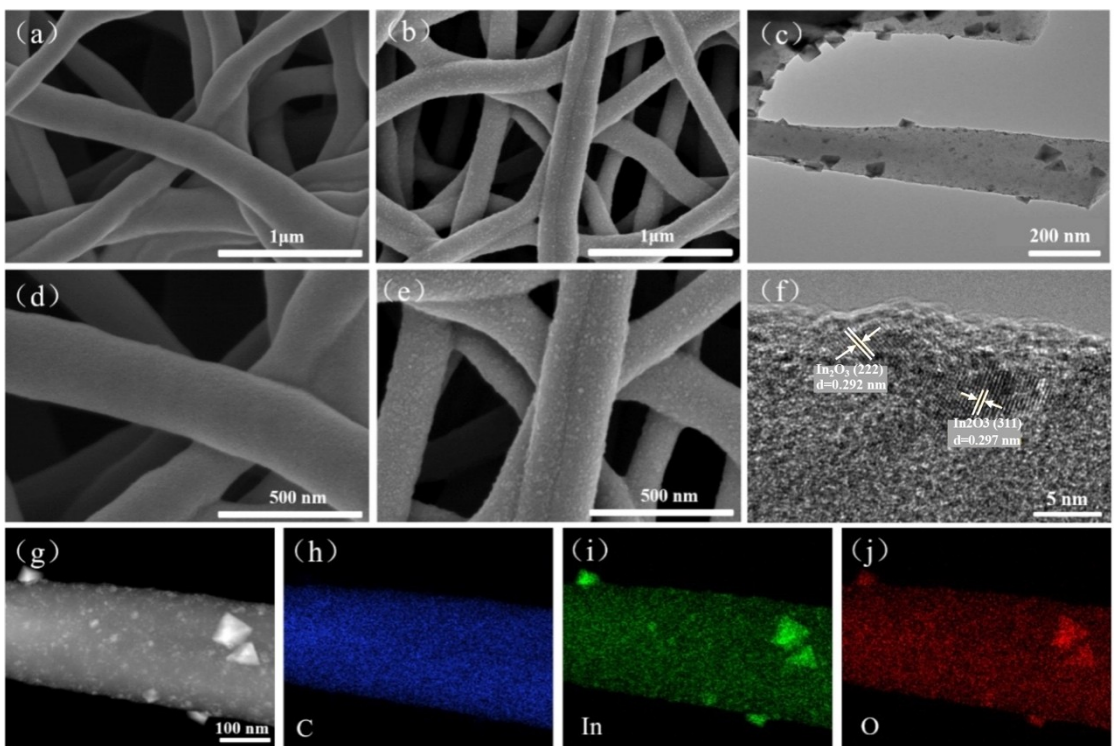
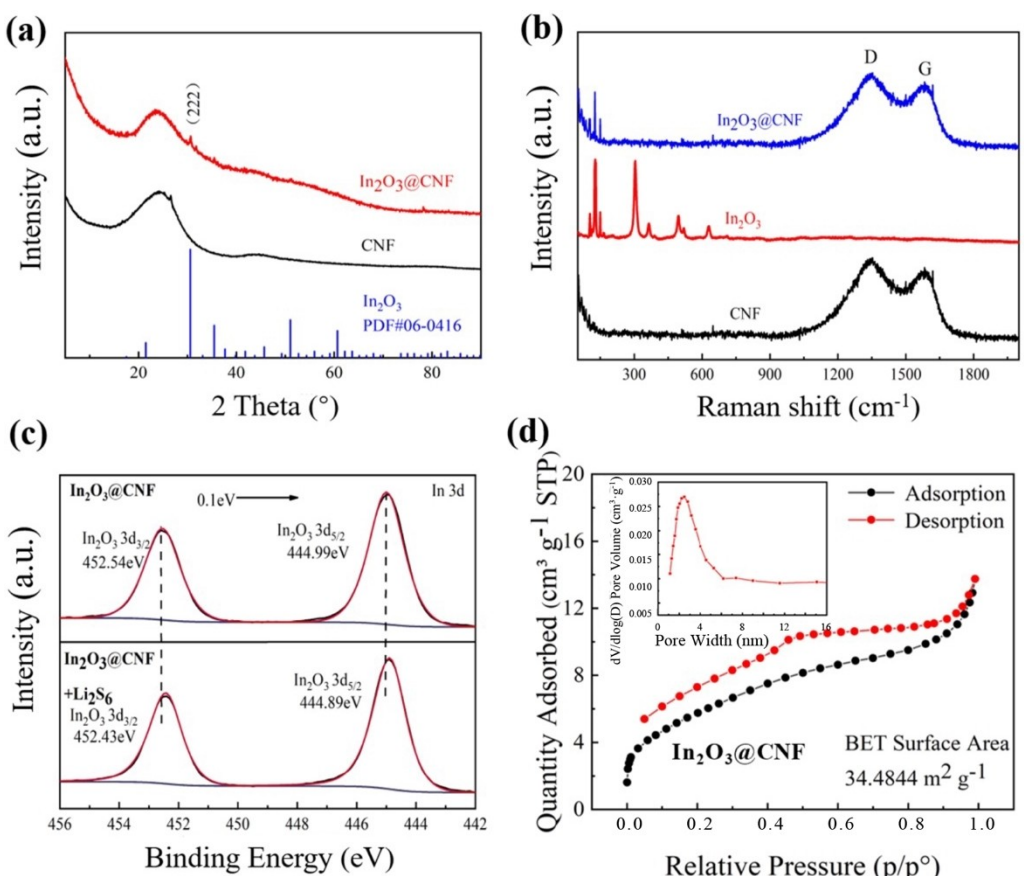


Figure 1. Schematic diagram of the preparation process and principle of  $\text{In}_2\text{O}_3@\text{CNF}$ .



**Figure 2.** (a) and (d) SEM images of CNF; (b) and (e) SEM images of  $\text{In}_2\text{O}_3$ @CNF; (c) TEM image of  $\text{In}_2\text{O}_3$ @CNF; (f) HRTEM image of  $\text{In}_2\text{O}_3$ @CNF; (g–j) EDS image of  $\text{In}_2\text{O}_3$ @CNF.



**Figure 3.** (a) XRD and (b) Raman patterns of CNF and  $\text{In}_2\text{O}_3$ @CNF (c) XPS spectra of In 3d for  $\text{In}_2\text{O}_3$ @CNF (d)  $\text{In}_2\text{O}_3$ @CNF  $\text{N}_2$  adsorption and desorption isotherm and pore size distribution curve.

successful synthesis of  $\text{In}_2\text{O}_3@\text{CNF}$ .<sup>[42]</sup> The high-resolution In 3d spectrum in Figure 3(c) shows two typical peaks at 452.5 eV and 444.9 eV, attributable to In 3d<sub>5/2</sub> and In 3d<sub>3/2</sub>, consistent with the In<sup>+3</sup> oxidation state of In<sup>[43]</sup> and confirming the presence of  $\text{In}_2\text{O}_3$ . After polysulfide adsorption, the In 3d peaks shift 0.1 eV towards lower binding energies, indicating interactions between  $\text{In}_2\text{O}_3$  and polysulfides that changed the electron cloud density.<sup>[44]</sup> In addition, the O 1s XPS spectra in Figure S3 proves the existence of the oxygen vacancy. From the O 1s XPS spectrum of  $\text{In}_2\text{O}_3@\text{CNF}$ , the peaks located at 530 eV, 531.6 eV, and 533.1 eV correspond to lattice oxygen (O<sub>l</sub>), oxygen vacancy (O<sub>v</sub>) and chemisorbed oxygen (O<sub>c</sub>), respectively.<sup>[45]</sup>

Figure 3(d) and Figure S4 show the N<sub>2</sub> adsorption-desorption isotherms and pore size distribution curves of  $\text{In}_2\text{O}_3@\text{CNF}$  and CNF. As can be seen from Figure 3(d), the adsorption-desorption isotherm of  $\text{In}_2\text{O}_3@\text{CNF}$  exhibits a hysteresis loop in the middle section, which is caused by capillary condensation where N<sub>2</sub> molecules condense and fill the mesopores under sub-atmospheric pressures. Since capillary condensation occurs first on the annular adsorbed film liquid surface on the pore walls, while desorption starts from the hemispherical meniscus liquid surface inside the pores, the adsorption and desorption branches do not coincide, resulting in a hysteresis loop of type IV adsorption isotherm.<sup>[46]</sup> The presence of a hysteresis loop in the medium pressure range indicates the material may contain mesopores. According to the inset in Figure 3(d), the pore size of  $\text{In}_2\text{O}_3@\text{CNF}$  is greater than 2 nm, evidencing the existence of mesopores. The total pore volume is 0.031 cm<sup>3</sup> g<sup>-1</sup>, larger than

that of CNF (0.019 cm<sup>3</sup> g<sup>-1</sup>). The presence of mesopores is presumed to be caused by the gas escape during thermal decomposition of nitrates. The specific surface areas calculated by BET method are 34.48 m<sup>2</sup> g<sup>-1</sup> and 15.45 m<sup>2</sup> g<sup>-1</sup> for  $\text{In}_2\text{O}_3@\text{CNF}$  and CNF, respectively. The increased surface area is due to the formation of  $\text{In}_2\text{O}_3$  particles. The existence of mesopores and high rough surface area facilitate faster electron transfer, and polysulfides can easily access the adsorption sites, restricting the shuttle effect.<sup>[47]</sup>

The electrochemical performance of lithium-sulfur batteries with no interlayer, CNF interlayer, and  $\text{In}_2\text{O}_3@\text{CNF}$  interlayer were tested. As shown in Figure 4(a), at a current density of 0.2 C (1 C = 1675 mAh g<sup>-1</sup>), the initial capacities of the batteries with three different configurations showed obvious differences. The battery with  $\text{In}_2\text{O}_3@\text{CNF}$  interlayer delivered an initial capacity of 1187.4 mAh g<sup>-1</sup>, much higher than CNF (823.3 mAh g<sup>-1</sup>) and no interlayer (677.2 mAh g<sup>-1</sup>). After 100 cycles, the discharge capacity of  $\text{In}_2\text{O}_3@\text{CNF}$  interlayer remained 920.5 mAh g<sup>-1</sup> with a capacity retention of 77.5%, superior to CNF (622 mAh g<sup>-1</sup> and 75.5%) and no interlayer (407.5 mAh g<sup>-1</sup> and 60.1%). The poor cycling of the cell without interlayer was due to the low conductivity of sulfur and serious polysulfide shuttle effect. Although the initial capacity was improved by adding CNF interlayer, the capacity decay was still severe because carbon materials only provide limited physical adsorption of polysulfides. The significantly enhanced initial capacity and capacity retention with  $\text{In}_2\text{O}_3@\text{CNF}$  interlayer demonstrates that  $\text{In}_2\text{O}_3$  can effectively adsorb polysulfides, accelerate their

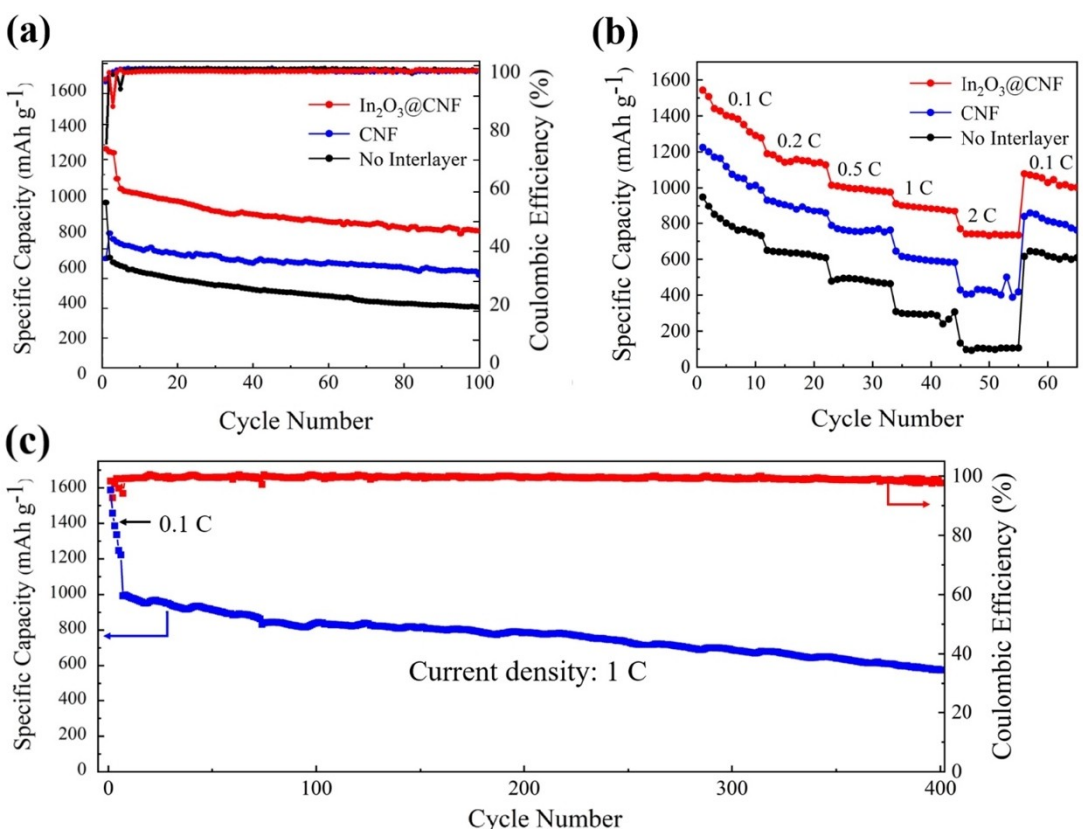


Figure 4. (a) Cycling performance and (b) Rate performance of CNF,  $\text{In}_2\text{O}_3@\text{CNF}$  and No interlayer. (c) Cycling performance of  $\text{In}_2\text{O}_3@\text{CNF}$  at 1 C.

conversion, and improve the sulfur utilization. Figure S5 shows the charge-discharge curves of  $\text{In}_2\text{O}_3@\text{CNF}$  battery at different cycles, where small capacity decay, stable voltage plateaus, and little potential hysteresis can be observed.

Figure 4(b) shows the rate performance at current densities of 0.1 C, 0.2 C, 0.5 C, 1 C and 2 C for Li–S batteries with three different configurations.  $\text{In}_2\text{O}_3@\text{CNF}$  exhibited the best rate capability compared to the other two. The initial capacities at all current densities were higher than the other two, indicating the lithium-sulfur battery with  $\text{In}_2\text{O}_3@\text{CNF}$  interlayer possesses excellent reversible specific capacity. Importantly, it could deliver a capacity of  $768.8 \text{ mAh g}^{-1}$  even at the high current density of 2 C, much higher than CNF ( $428.5 \text{ mAh g}^{-1}$ ) and without interlayer ( $133.9 \text{ mAh g}^{-1}$ ). Meanwhile, when the current density switched back to 0.1 C, the cell could discharge continuously and steadily, and the capacity recovered to  $1078.3 \text{ mAh g}^{-1}$ , corresponding to 70.86% of its initial capacity, displaying excellent electrochemical reversibility and stability. Additionally, as shown in Figure S6, distinct charge-discharge plateaus can be observed for the cell with  $\text{In}_2\text{O}_3@\text{CNF}$  interlayer despite the continuously changing current densities. More impressively, after 0.1 C activation, the  $\text{In}_2\text{O}_3@\text{CNF}$  interlayer battery exhibited stable cycling at a current density of 1 C with an initial capacity of  $997 \text{ mAh g}^{-1}$  (Figure 4(c)). After 400 cycles, it maintained a reversible discharge capacity of  $589.1 \text{ mAh g}^{-1}$ , with a capacity decay rate per cycle of only 0.1% and a coulombic efficiency close to 100%. Figure S7(a) shows the first cycle charge-discharge profiles of lithium–sulfur batteries with three different configurations at 0.2 C.  $\Delta E$  refers to the median voltage difference. By calculation and comparison, the cell with  $\text{In}_2\text{O}_3@\text{CNF}$  interlayer has the smallest  $\Delta E$  value, indicating improved reaction kinetics and lowered polarization. The enlarged schematic of the discharge plateaus in Figure S7(b) clearly shows  $\text{In}_2\text{O}_3@\text{CNF}$  has the smallest overpotential. The sulfur cathode capacity highly depends on the conversion of soluble  $\text{Li}_2\text{S}_4$  to solid  $\text{Li}_2\text{S}_2$ , which is closely related to the overpotential. The lowest overpotential of  $\text{In}_2\text{O}_3@\text{CNF}$  suggests  $\text{In}_2\text{O}_3$  plays a role in accelerating the solid-liquid conversion of polysulfides, facilitating the transformation of soluble  $\text{Li}_2\text{S}_4$  and thus improving the charge-discharge capacity of the battery. Further long cycle tests with high area capacity were done to verify its possibility in practical applications. As shown in Figure S8, at a current density of 0.1 C, the cell containing the intermediate layer exhibits a high initial capacity of  $888 \text{ mAh g}^{-1}$ . And it still has a capacity of  $569 \text{ mAh g}^{-1}$  after 100 cycles. The capacity retention rate is 64%. The electrode loading was about  $6 \text{ mg cm}^{-2}$ . Meanwhile, we compare the work of some intermediate layers applied to Li–S batteries. (Table S1) Obviously, it is competitive in terms of high S content cycling performance.

Li–S batteries were assembled using CNF and  $\text{In}_2\text{O}_3@\text{CNF}$  respectively as interlayers, and the effect of  $\text{In}_2\text{O}_3@\text{CNF}$  on the electrochemical performance was analyzed by cyclic voltammetry characterization. Figure S9(a) shows the CV curves without interlayer and with CNF and  $\text{In}_2\text{O}_3@\text{CNF}$  interlayers at a scan rate of  $0.1 \text{ mV s}^{-1}$  and voltage range of  $1.7 \text{ V}–2.8 \text{ V}$ . In the cathodic scan, the reduction peaks represent the reduction of

$\text{S}_8$  to  $\text{Li}_2\text{S}_4$ , and further reduction of  $\text{Li}_2\text{S}_4$  to  $\text{Li}_2\text{S}/\text{LiS}$ . In the anodic scan, the oxidation peaks correspond to the oxidation of  $\text{Li}_2\text{S}_2/\text{Li}_2\text{S}$  to soluble polysulfides, and partial polysulfides are further oxidized to  $\text{S}_8$ . Compared to no interlayer and CNF interlayer,  $\text{In}_2\text{O}_3@\text{CNF}$  exhibited much higher peak currents, indicating lower electrochemical polarization and faster redox reactions for the cell with  $\text{In}_2\text{O}_3@\text{CNF}$  interlayer. Furthermore, as shown in Figure S9(b), the CV curves of  $\text{In}_2\text{O}_3@\text{CNF}$  battery for the first three cycles almost overlap at a scan rate of  $0.1 \text{ mV s}^{-1}$ , demonstrating the highly reversible cycling of the cell with the  $\text{In}_2\text{O}_3@\text{CNF}$  interlayer.

To further reveal the electrochemical behavior of the  $\text{In}_2\text{O}_3@\text{CNF}$  interlayer in Li–S battery operation, the CV curves were tested within a voltage window of  $1.7$ – $2.8 \text{ V}$ , as shown in Figure S10. There are two typical cathodic peaks,  $\sim 2.0 \text{ V}$  and  $\sim 2.3 \text{ V}$ , attributed to the production of polysulfide intermediates and the discharge product  $\text{Li}_2\text{S}$ , respectively. Obviously, the redox peaks of the electrodes with  $\text{In}_2\text{O}_3@\text{CNF}$  interlayer show the largest response current, which suggests that  $\text{In}_2\text{O}_3@\text{CNF}$  can accelerate the redox kinetics. This is due to the catalytic effect of In and oxygen defects in  $\text{In}_2\text{O}_3@\text{CNF}$ . In order to accurately analyze the nucleation and dissociation reactions of  $\text{Li}_2\text{S}$ , Tafel curves of the corresponding redox peaks were plotted. The  $\text{Li}_2\text{S}$  dissociation degree peak corresponds to the anodic peak, and the Tafel slopes for the  $\text{In}_2\text{O}_3@\text{CNF}$  and CNF fits are  $108 \text{ mV dec}^{-1}$  and  $138 \text{ mV dec}^{-1}$ . For nucleation with  $\text{Li}_2\text{S}$  and formation of polysulfide intermediates corresponding cathodic peaks. The Tafel slopes for the  $\text{In}_2\text{O}_3@\text{CNF}$  and CNF fits were  $67.84 \text{ mV dec}^{-1}$  and  $140, 126 \text{ mV dec}^{-1}$ . (Details are shown in Figure S11). The Tafel slopes with added  $\text{In}_2\text{O}_3@\text{CNF}$  interlayer are all lower than those with added CNF interlayer. Since smaller Tafel slopes imply faster electrokinetic processes, it can be confirmed that the  $\text{In}_2\text{O}_3@\text{CNF}$  interlayer accelerates the  $\text{Li}_2\text{S}$  nucleation and dissociation reactions. Symmetric cells were assembled with  $0.2 \text{ M } \text{Li}_2\text{S}_6$  as electrolyte by placing a  $\text{In}_2\text{O}_3@\text{CNF}$  interlayer (or CNF interlayer) on both sides of the separator and tested at a voltage range of  $-0.8$  to  $0.8 \text{ V}$  at a scan rate of  $10 \text{ mV s}^{-1}$ . As shown in Figure S12, the CV curve of the symmetric cell with  $\text{In}_2\text{O}_3@\text{CNF}$  exhibits smaller voltage separation than CNF, confirming the redox kinetics of polysulfide conversion in the presence of  $\text{In}_2\text{O}_3@\text{CNF}$ .

To further understand the role of different interlayers in accelerating the electrocatalytic conversion of polysulfides, CV measurements of CNF and  $\text{In}_2\text{O}_3@\text{CNF}$  were conducted at different scan rates from  $0.1 \text{ mV s}^{-1}$  to  $0.5 \text{ mV s}^{-1}$  to analyze the lithium-ion diffusion kinetics as shown in Figure 5(a) (details of lithium-ion diffusion coefficient calculation can be found in the supporting information and Figure S13). The calculated  $D_{\text{Li}}$  values are  $2.87 \times 10^{-10} \text{ cm}^2 \text{s}^{-1}$  for  $\text{In}_2\text{O}_3@\text{CNF}$  and  $2.21 \times 10^{-10} \text{ cm}^2 \text{s}^{-1}$  for CNF.  $I_p$  shows a linear relationship with the square root of scan rate  $v^{1/2}$ . As shown in Figure 5(b), the slope of the reduction peak for  $\text{In}_2\text{O}_3@\text{CNF}$  is greater than that of CNF. During battery cycling, the precipitation of insulating  $\text{Li}_2\text{S}_2/\text{Li}_2\text{S}$  can decrease lithium-ion transport. However, the presence of CNF scaffold and  $\text{In}_2\text{O}_3$  in the  $\text{In}_2\text{O}_3@\text{CNF}$  interlayer increases catalytic active sites, prevents insulating layer formation, and thus improves lithium ion diffusion kinetics and

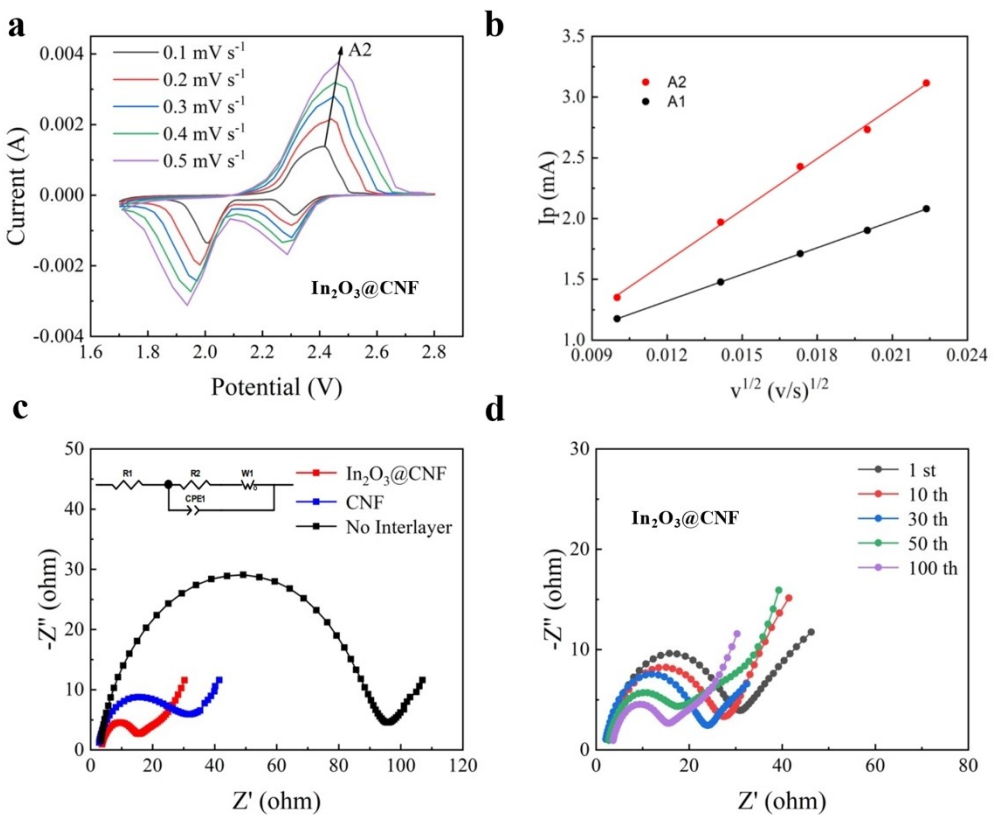


**Figure 5.** (a) Cyclic voltammery curves with  $\text{In}_2\text{O}_3@\text{CNF}$  interlayer at different sweep speeds; (b) Relationship between the square root of the scanning speed of each peak potential and the peak current; (c) EIS diagram of lithium–sulfur batteries with CNF and  $\text{In}_2\text{O}_3@\text{CNF}$  interlayer and No interlayer after 100 cycles; (d) EIS diagram of lithium–sulfur batteries with  $\text{In}_2\text{O}_3@\text{CNF}$  interlayer after different cycles.

polysulfide conversion dynamics.<sup>[48]</sup> To further confirm the role of the  $\text{In}_2\text{O}_3@\text{CNF}$  in facilitating Li-ion diffusion, the diffusion kinetics of  $\text{Li}^+$  solid-state diffusion in the  $\text{In}_2\text{O}_3@\text{CNF}$  and CNF were investigated via GITT. The diffusion coefficient of  $\text{In}_2\text{O}_3@\text{CNF}$  at different stages is overall higher than that of CNF, which further indicated reduced hysteresis and better kinetic properties. (Figure S14,15)

In addition, electrochemical impedance (EIS) tests were performed on lithium–sulfur batteries incorporating three intermediate layers to probe the interfacial charge transfer behaviors. Figure 5(c) shows the EIS curve for three different battery configurations after 100 cycles. The charge transfer impedance ( $R_2$ ) value of the Li–S battery without interlayer is  $92.9 \Omega$ , the  $R_2$  value with CNF interlayer is  $30.2 \Omega$ , and the  $R_2$  value with  $\text{In}_2\text{O}_3@\text{CNF}$  is even lower, which is only  $12.2 \Omega$ . It indicates that the charge transfer between  $\text{In}_2\text{O}_3@\text{CNF}$  interlayer and polysulfide is faster. Figure 5(d) and Figure S16 show the EIS curves of Li–S batteries containing CNF and  $\text{In}_2\text{O}_3@\text{CNF}$  interlayers, respectively, after different numbers of cycling cycles, and the impedances of both decrease with the increase of the number of cycling cycles. More importantly, the impedance of  $\text{In}_2\text{O}_3@\text{CNF}$  is smaller than that of CNF at different number of cycles, which indicates that  $\text{In}_2\text{O}_3$  accelerates the conversion of polysulfides as well as the lithium-ion transport in the battery cycle.

In order to test the polysulfide adsorption capability of  $\text{In}_2\text{O}_3@\text{CNF}$ , the same mass of CNF and  $\text{In}_2\text{O}_3@\text{CNF}$  were added into the prepared  $\text{Li}_2\text{S}_6$  solution. As shown in Figure S17, the original  $\text{Li}_2\text{S}_6$  solution was yellow. After 12 h, the solution with CNF added turned light yellow, while the solution with  $\text{In}_2\text{O}_3@\text{CNF}$  added became clear. By comparison,  $\text{In}_2\text{O}_3@\text{CNF}$  interlayer showed the best adsorption capability, indicating  $\text{In}_2\text{O}_3$  has polysulfide adsorption capability to suppress the shuttle effect. To further confirm the suppression effect of  $\text{In}_2\text{O}_3@\text{CNF}$  interlayer on polysulfide shuttling, Li–S batteries without interlayer, with CNF interlayer, and with  $\text{In}_2\text{O}_3@\text{CNF}$  interlayer were cycled at 0.2 C for 100 cycles, disassembled, and the separators close to lithium metal were characterized by SEM. As shown in Figure 6, some  $\text{Li}_2\text{S}/\text{Li}_2\text{S}_2$  particles were observed on the separators of batteries without interlayer (a) and with CNF interlayer (b), while fewer particles were on the separator with  $\text{In}_2\text{O}_3@\text{CNF}$  interlayer (c). Additionally, the sulfur mapping images clearly show less sulfur distribution on the separator with  $\text{In}_2\text{O}_3@\text{CNF}$  interlayer. EDS analysis further indicates 29.06% and 14.38% sulfur content on the separators without and with CNF interlayer, compared to only 6.61% for  $\text{In}_2\text{O}_3@\text{CNF}$  interlayer. These results demonstrate significantly reduced shuttled polysulfides to lithium metal surface in the cell with  $\text{In}_2\text{O}_3@\text{CNF}$  interlayer, confirming the strong polysulfide adsorption capability of  $\text{In}_2\text{O}_3$  particles and effective suppression of the shuttle effect in Li–S batteries.

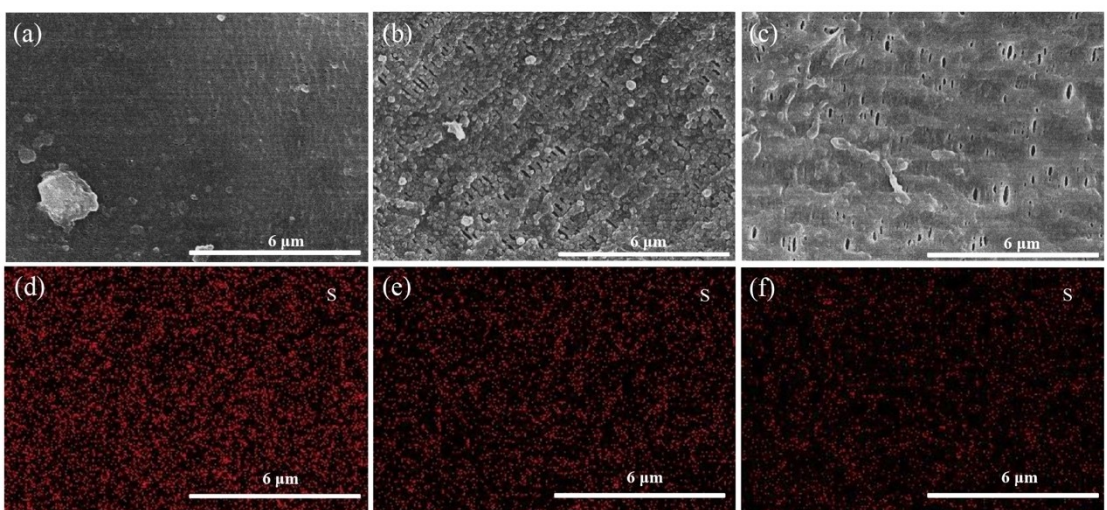


**Figure 6.** SEM and sulfur distribution of diaphragm after 100 cycles (a) (d) No interlayer; (b) (e) with the CNF interlayer; (c) (f) with the  $\text{In}_2\text{O}_3@\text{CNF}$  interlayer.

### 3. Conclusions

$\text{In}_2\text{O}_3@\text{CNF}$  composite interlayer was successfully prepared using electrospinning and applied to Li-S batteries. The oxygen vacancies in  $\text{In}_2\text{O}_3@\text{CNF}$  have high electronic activity around the defects, which can chemically adsorb polysulfides and form chemical bonds. This effectively suppresses the shuttle effect and accelerates the conversion reaction of polysulfides. The lithium-sulfur battery with  $\text{In}_2\text{O}_3@\text{CNF}$  interlayer delivers an excellent initial discharge capacity of  $1187.4 \text{ mAh g}^{-1}$  at  $0.2 \text{ C}$ , and maintains  $920.5 \text{ mAh g}^{-1}$  after 100 cycles. At  $1 \text{ C}$ , it not only exhibits an initial discharge capacity of  $997 \text{ mAh g}^{-1}$ , but also outstanding cycling stability (nearly 100% coulombic efficiency over 400 cycles). Thus, this study provides a novel approach for fabricating high-energy and stable Li-S batteries.

### Author Contributions

**Yibo Xiao:** Conceptualization, Formal analysis, Data curation, Writing- Original draft preparation.

**Ting Ma:** Formal analysis, Data curation and Editing, Writing-Original draft preparation.

**Xiaoxia Lv:** Data curation.

**Haixia Yue:** Data curation.

**Yixin Huang:** Data curation and Editing.

**Xin Li:** Data curation and Editing.

**Na He:** Validation and Analysis.

**Changzhen Zhan:** Editing, Funding acquisition.

**Yu Bai:** Writing - Reviewing and Editing.

**Ding Nan:** Writing - Reviewing and Editing, Funding acquisition.

### Acknowledgements

The financial supports for this work are the National Natural Science Foundation of China (No. 52202040), the Inner Mongolia Major Science and Technology Project (no. 2020ZD0024), Local Science and Technology Development Project of the Central Government (no. 2021ZY0006, 2022ZY0011), the Project of Innovation Research in Postgraduate in Inner Mongolia (B20231023Z), Inner Mongolia Autonomous Region key Research and Technological Achievements Transformation Plan Project (no. 2023YFHH0063), Graphite and Graphene New Materials Discipline Team of Inner Mongolia University of Technology (No. PY202066) and Natural Science Foundation of Inner Mongolia (no.2024LHMS05046).

### Conflict of Interests

The authors declare no conflict of interest.

### Data Availability Statement

The data that support the findings of this study are available from the corresponding author upon reasonable request.

**Keywords:** Lithium–sulfur battery • Indium oxide • Interlayer • Electrospinning

- [1] S. H. Chung, A. Manthiram, *Adv. Mater.* **2019**, *31*, 1901125.
- [2] X. Chi, M. Li, J. Di, P. Bai, L. Song, X. Wang, F. Li, S. Liang, J. Xu, J. Yu, A. highly stable, *Nature* **2021**, *592*, 551–557.
- [3] J. Wang, J. Zhang, J. Wu, M. Huang, L. Jia, L. Li, Y. Zhang, H. Hu, F. Liu, Q. Guan, *Adv. Mater.* **2023**, *35*, 2302828.
- [4] J. Wang, J. Zhang, Y. Zhang, H. Li, P. Chen, C. You, M. Liu, H. Lin, S. Passerini, *Adv. Mater.* **2024**, *36*, 2402792.
- [5] S. Liu, X. Ji, N. Piao, J. Chen, N. Eidson, J. Xu, P. Wang, L. Chen, J. Zhang, T. Deng, *Angew. Chem. Int. Ed.* **2021**, *60*, 3661–3671.

- [6] A. Manthiram, Y. Fu, S.-H. Chung, C. Zu, Y.-S. Su, *Chem. Rev.* **2014**, 114, 11751–11787.
- [7] J. Wang, L. Jia, H. Liu, C. Wang, J. Zhong, Q. Xiao, J. Yang, S. Duan, K. Feng, N. Liu, *ACS Appl. Mater. Interfaces* **2020**, 12, 12727–12735.
- [8] J. Wang, H. Liu, J. Zhang, Q. Xiao, C. Wang, Y. Zhang, M. Liu, Q. Kang, L. Jia, D. Wang, *Energy Storage Mater.* **2024**, 67, 103289.
- [9] C. P. Yang, S. Xin, Y. X. Yin, H. Ye, J. Zhang, Y. G. Guo, *Angew. Chem.* **2013**, 125, 8521–8525.
- [10] L. Hencz, H. Chen, Z. Wu, S. Qian, S. Chen, X. Gu, X. Liu, C. Yan, S. Zhang, *Highly branched amylopectin binder for sulfur cathodes with enhanced performance and longevity*, in: *Exploration*, vol. 2, Wiley Online Library, 2022, pp. 20210131.
- [11] J. Wang, L. Jia, J. Zhong, Q. Xiao, C. Wang, K. Zang, H. Liu, H. Zheng, J. Luo, J. Yang, *Energy Storage Mater.* **2019**, 18, 246–252.
- [12] S. S. Zhang, *Energies* **2014**, 7, 4588–4600.
- [13] G. Li, S. Wang, Y. Zhang, M. Li, Z. Chen, J. Lu, *Adv. Mater.* **2018**, 30, 1705590.
- [14] Z. Han, S. Li, Y. Wu, C. Yu, S. Cheng, J. Xie, *J. Mater. Chem. A* **2021**, 9, 24215–24240.
- [15] L. Li, H. Tu, J. Wang, M. Wang, W. Li, X. Li, F. Ye, Q. Guan, F. Zhu, Y. Zhang, *Adv. Funct. Mater.* **2023**, 33, 2212499.
- [16] X. Yu, J. Zhao, R. Lv, Q. Liang, C. Zhan, Y. Bai, Z.-H. Huang, W. Shen, F. Kang, *J. Mater. Chem. A* **2015**, 3, 18400–18405.
- [17] X. Yu, J. Deng, R. Lv, Z.-H. Huang, B. Li, F. Kang, *Energy Storage Mater.* **2019**, 20, 14–23.
- [18] Y. Wang, R. Zhang, J. Chen, H. Wu, S. Lu, K. Wang, H. Li, C. J. Harris, K. Xi, R. V. Kumar, *Adv. Energy Mater.* **2019**, 9, 1900953.
- [19] Z. Cui, C. Zu, W. Zhou, A. Manthiram, J. B. Goodenough, *Adv. Mater.* **2016**, 28, 6926–6931.
- [20] Y.-S. Su, A. Manthiram, *Nat. Commun.* **2012**, 3, 1166.
- [21] W. Shin, L. Zhu, H. Jiang, W. F. Stickle, C. Fang, C. Liu, J. Lu, X. Ji, *Mater. Today* **2020**, 40, 63–71.
- [22] J. Lian, W. Guo, Y. Fu, *J. Am. Chem. Soc.* **2021**, 143, 11063–11071.
- [23] F. Shi, C. Chen, Z.-L. Xu, *Advanced Fiber Materials* **2021**, 3, 275–301.
- [24] X. Li, W. Chen, Q. Qian, H. Huang, Y. Chen, Z. Wang, Q. Chen, J. Yang, J. Li, Y. W. Mai, *Adv. Energy Mater.* **2021**, 11, 2000845.
- [25] X. Zhang, L. Ji, O. Toprakci, Y. Liang, M. Alcoutabi, *Polym. Rev.* **2011**, 51, 239–264.
- [26] L. Liu, A. Liao, L. Lin, Y. Huang, Y. Zhang, Y. Liu, G. Gao, J. Lin, B. Sa, L. Wang, *J. Power Sources* **2024**, 608, 234642.
- [27] M. Zheng, Z. Luo, Y. Song, M. Zhou, C. Guo, Y. Shi, L. Li, Q. Sun, B. Shi, Z. Yi, *J. Power Sources* **2023**, 580, 233445.
- [28] G. Ma, Z. Wen, J. Jin, M. Wu, X. Wu, J. Zhang, *J. Power Sources* **2014**, 267, 542–546.
- [29] K. Wu, Y. Hu, Z. Cheng, P. Pan, L. Jiang, J. Mao, C. Ni, X. Gu, Z. Wang, *J. Membr. Sci.* **2019**, 592, 117349.
- [30] G. Liang, J. Wu, X. Qin, M. Liu, Q. Li, Y.-B. He, J.-K. Kim, B. Li, F. Kang, *ACS Appl. Mater. Interfaces* **2016**, 8, 23105–23113.
- [31] J. M. Choi, R. Saroha, J. S. Kim, M. R. Jang, J. S. Cho, *J. Power Sources* **2023**, 559, 232632.
- [32] Z. Li, C. Zhou, J. Hua, X. Hong, C. Sun, H. W. Li, X. Xu, L. Mai, *Adv. Mater.* **2020**, 32, 1907444.
- [33] J. Wu, Y. Dai, Z. Pan, D. Huo, T. Wang, H. Zhang, J. Hu, S. Yan, *Appl. Surf. Sci.* **2020**, 510, 145529.
- [34] C. Du, J. Wu, P. Yang, S. Li, J. Xu, K. Song, *Electrochim. Acta* **2019**, 295, 1067–1074.
- [35] W. S. Seo, H. H. Jo, K. Lee, J. T. Park, *Adv. Mater.* **2003**, 15, 795–797.
- [36] W. Hua, H. Li, C. Pei, J. Xia, Y. Sun, C. Zhang, W. Lv, Y. Tao, Y. Jiao, B. Zhang, *Adv. Mater.* **2021**, 33, 2101006.
- [37] W.-H. Ho, C.-F. Li, H.-C. Liu, S.-K. Yen, *J. Power Sources* **2008**, 175, 897–902.
- [38] G. Han, X. Wang, J. Yao, M. Zhang, J. Wang, *Nanomaterials* **2020**, 10, 177.
- [39] T. Wang, Z. Shi, F. Wang, S. Cui, Z. Zhang, W. Liu, Y. Jin, *ACS Appl. Mater. Interfaces* **2024**, 16, 18937–18948.
- [40] L. Fan, M. Li, X. Li, W. Xiao, Z. Chen, J. Lu, *Joule* **2019**, 3, 361–386.
- [41] Y. Mo, K. Yang, J. Lin, M. Liu, G. Ye, J. Yu, *J. Mater. Chem. A* **2023**, 11, 6349–6360.
- [42] H. Zhao, H. Yin, X.-X. Yu, W. Zhang, C. Li, M.-Q. Zhu, *J. Alloys Compd.* **2018**, 735, 319–326.
- [43] Q. Zhao, G. Zhuang, Y. Zhao, L. Yang, J. Zhao, *New J. Chem.* **2021**, 45, 6773–6779.
- [44] P. Zeng, M. Chen, S. Jiang, Y. Li, X. Xie, H. Liu, X. Hu, C. Wu, H. Shu, X. Wang, *ACS Appl. Mater. Interfaces* **2019**, 11, 22439–22448.
- [45] J. Qin, R. Wang, Z. Yuan, P. Xiao, D. Wang, *Nano Res.* **2024**, 1–9.
- [46] E. Alhajji, W. Wang, W. Zhang, H. N. Alshareef, *ACS Appl. Mater. Interfaces* **2020**, 12, 18833–18839.
- [47] F. Hu, H. Peng, T. Zhang, W. Shao, S. Liu, J. Wang, C. Wang, X. Jian, *J. Energy Chem.* **2021**, 58, 115–123.
- [48] Y. You, Y. Ye, M. Wei, W. Sun, Q. Tang, J. Zhang, X. Chen, H. Li, J. Xu, *Chem. Eng. J.* **2019**, 355, 671–678.

Manuscript received: November 12, 2024

Revised manuscript received: December 29, 2024

Accepted manuscript online: January 2, 2025

Version of record online: January 13, 2025